High-surface-area functionalized nanolaminated membranes for energy-efficient nanofiltration and desalination in forward osmosis

Wensen Wang, Nicolas Onofrio, Eddy Petit, Bonito Aristide Karamoko, Huali Wu, Jiefeng Liu, Ji Li, Kun Qi, Yang Zhang, Christel Gervais, et al.

High Surface Area Functionalized Nanolaminated Membranes For Energy Efficient Nanofiltration And Desalination In Forward Osmosis

Wensen Wang[1], Nicolas Onofrio[1], Eddy Petit[1], Bonito Aristide Karamoko[1], Huali Wu[1], Jiefeng Liu[1], Ji Li[1,2], Kun Qi[1], Yang Zhang[1,3], Christel Gervais,[4,5] Luc Lajaunie[6,7], Chrystelle Salameh[1], Philippe Miele[1,4], Zhiyuan Zeng [8,9], Damien Voiry[1]*

[1] *Institut Européen des Membranes, IEM, UMR 5635, Université Montpellier, ENSCM, CNRS, Montpellier 34000, France*

[2]*College of Bioresources and Materials Engineering, Shaanxi University of Science & Technology, Xi'an 710021, P. R. China*

[3] *Key Laboratory of Optoelectronic Devices and Systems of Ministry of Education and Guangdong Province, College of Optoelectronic Engineering, Shenzhen University, Shenzhen, 518000, China*

[4] *Institut Universitaire de France (IUF), 1 rue Descartes, 75231 Paris Cedex 05*

[5] *Sorbonne Université, Collège de France, Laboratoire de Chimie de la Matière Condensée de Paris (LCMCP), 4 place Jussieu, 75252 Paris cedex 05, France.*

[6] *Departamento de Ciencia de los Materiales e Ingeniería Metalúrgica y Química Inorgánica, Facultad de Ciencias, Universidad de Cádiz, Campus Río San Pedro S/N, Puerto Real, 11510, Cádiz, Spain*

[7] *Instituto Universitario de Investigación de Microscopía Electrónica y Materiales (IMEYMAT), Facultad de Ciencias, Universidad de Cádiz, Campus Río San Pedro S/N, Puerto Real 11510, Cádiz, Spain*

[8]*Department of Materials Science and Engineering, City University of Hong Kong, Hong Kong 999077, P. R. China*

[9]*Shenzhen Research Institute, City University of Hong Kong, Shenzhen 518057, China*

Abstract

Stacking two-dimensional (2D) nanosheets into laminar membranes to create nanochannels has attracted widespread attention at fundamental and practical levels for separation technology. Constructing space-tunable and long-term stable sub-nanometer channels provide original systems for nanofluidic investigations and accurate molecular sieving. Here, we report a scalable strategy for the preparation of non-swelling covalently functionalized molybdenum disulfide (MoS_2) membranes with tunable cohesion energy and interlayer space from 3.5 to

7.7 Å, depending on the nature of the functional groups attached to the MoS_2 nanosheets. We evaluated the relationship between the capillary width, the surface chemistry, the stacking disorder and the sieving behaviors of the membranes in forwards osmosis (FO). By combining experimental investigations and numerical simulations, we identified that the functionalization with aryl groups induces the formation of a capillary width of 7.1 Å and interlayer stiffness as low as 5.6 eV $Å^{-2}$, leading to controlled stacking defects. We report the fabrication of membranes up to 45 cm^2, which demonstrate a salt rejection as high as 94.2% for a continuous operating time of 7 days. Our work presents a desalination strategy in FO with a specific energy consumption (SEC) of 4×10^{-3} kWh m^{-3}, which compares favorably with commercial FO membranes.

Introduction

The construction of selectively permeable membranes with sub-nanometer channels has gained attention for artificial bionics and molecular sieving by taking advantage of the sub-nanometer size of the pores formed between two successive nanosheets. Two-dimensional nanolaminates are regarded from both fundamental and practical points of view as mimicking systems of the biological protein transport channels and building blocks of nanofiltration membranes[1,2]. In nanolaminated membranes, mass transport typically occurs within the physical gap between the layers defined as the interlayer space or the capillary width. The fabrication of 2D sub-nanometer channels with controlled dimensionality and chemistry of the interlayer space has therefore emerged as a mature topic in the field of 2D materials[3-5]. The practical demonstration of nanolaminate membranes has not been achieved due to two main bottlenecks, which are (i) the intrinsic instability of the interlayer space and (ii)

the difficulty in fabricating pinhole-free membranes on a large scale with controlled thickness[6-8]. Currently, the most widely studied 2D building block of nanolaminate membranes is graphene oxide (GO), which forms free spaces of around 5 Å in dry condition. This allows a narrow molecular sieve size with sharp molecular cut-off for rejecting large molecules and ions at the expense of the water flux[9]. Although the space size can be modulated by encapsulating GO membrane into epoxy under different humidity, the process is rather complex and prevents realistic applications[10]. Other strategies for controlling the pore size of the nanolaminates include ion coordination[11], polymer intercalation[12], crosslinking[13]. Inevitable swelling occurs in pristine GO membranes when it is operated in an aqueous solution, which dramatically increases the interlayer spacing, leading to a rapid degradation of the sieving performance[14-16]. Besides GO, MoS_2 and MXene nanosheets are alternative building block candidates for the construction of 2D nanochannels[17-20]. MoS_2 laminated membranes have shown outstanding water permeation in reversed osmosis (RO) and the improved stability compared to GO and MXene membranes[21,22]. Unfortunately, the molecular cutoff of MoS_2 membranes depends on the presence of intercalated water molecules in the laminated structure[23]. We have recently reported a facile strategy to modify the surface chemistry of the MoS_2 nanosheets and tune the interlayer space[24]. Although the vast majority of the efforts have focused on membranes for RO applications, forward osmosis (FO) is regarded as a strategy to reduce the energy footprint associated with water purification processes. To date, only few studies have however focused on the production and testing membranes with sizes greater than 1 cm^2 due to the difficulty in controlling the integrity of the membrane structures over large area (swelling, delamination, formation of pinholes)[24-26].

Here, using MoS_2 nanosheets as building units, we adopted a chemical

functionalization strategy to prepare FO membranes with controlled interlayer space and interlayer stiffness in order to tailor the interlayer space and the stacking disorder in the nanolaminated structure. The membranes are found to be resistant against swelling, while the interlayer space can be adjusted with ångström precision. We demonstrated the fabrication of membranes with thickness from 100 nm up to 1 µm and dimensions as large as 45 cm^2. The membranes achieved a water flux as high as 12 LMH with molecular cutoff of 180 Da and a salt rejection as high as 94.2%. When tested against desalination, the functionalized MoS_2 FO membranes demonstrated superior salt rejection performance for 7 days without significant loss of the water flux compared with GO-based membranes and commercial polymer FO membranes. The nanofluidic behavior in various channels has been studied using physical characterizations and molecular dynamic simulations to unravel the size entanglements of the surface chemistry, the sub-nanometer interlayer space and the disorder of the stacking of the nanosheets in the laminated structure. We finally evaluated the energy consumption of our filtration system and found that the MoS_2 nanolaminate membranes may allow for a lower electrical power consumption compared to commercial FO membranes thus opening avenues for practical applications of nanolaminate FO membranes.

Characterization of Nanolaminated MoS_2 Membranes

Molybdenum disulfide nanosheets were exfoliated in water from a bulk crystal and further functionalized using alternatively organohalides or diazonium salts in order to covalently attach alkyl and aryl functional groups, respectively[27]. Six types of molecules were selected offering different sizes and polarities. The functionalized MoS_2 nanosheets were first observed using electron microscopy in order to confirm the presence of attached functional groups and the crystallinity of the nanosheets (**Fig. 1a,**

b). The functionalized nanosheets were then characterized by performing Attenuated total reflectance Fourier-transformed infrared (ATR-FTIR), Raman and ^{13}C nuclear magnetic resonance (^{13}C NMR) spectroscopies as well as thermogravimetric analysis (TGA) (Supplementary Note 1). **Figures 2a, b** show the chemical shifts of functionalized MoS_2 nanosheets compared with those of the pristine organohalide or diazonium salt reagents. The ^{13}C signals of the aliphatic carbon (α-C) at -3.7 ppm[28] and 115.3 ppm[29] for ethyl iodoacetate and 4-bromobenzenediazonium respectively disappear after functionalization and are shifted around 46 ppm and 126 ppm. The significant perturbation of the α-C chemical shifts suggests a new chemical environment, which is attributed to the formation of S-C bonds.

The membranes were fabricated by vacuum filtering of the suspension of MoS_2 nanosheets on a porous support and the membrane thickness was adjusted between 100 nm and 1 μm (Supplementary Figure 5). The ordered interstitial structure was confirmed by the cross-section view of one typical functionalized membrane using scanning electron microscopy (SEM) and X-ray diffraction (XRD) (**Fig. 1c** and **Fig. 2c, d**).

Compared to pristine MoS_2 nanolaminates, which display an intense (002) peak at ~14.2°, the peaks of functionalized membranes shift to lower angles corresponding to an increased interlayer space between the nanosheets. The capillary width was estimated by subtracting 6.15 Å corresponding to the Mo-Mo distance between two successive layers of MoS_2 in a bulk crystal. We obtained capillary width of 3.6 Å, 4.8 Å, 5.3 Å, 6.9 Å, 6.5 Å, and 7.1 Å for C_2-, C_3-, Ace-, Ben-, C_3OH- and Aryl-functionalized MoS_2, respectively. Our XRD analyses therefore suggest that the interlayer spacing can be fine-tuned to ångström accuracy by employing different sizes

of functional groups. To visually observe the increase of the interlayer space, we measured the evolution of the membrane thickness before and after functionalization (**Fig. 2e** and Supplementary Figure 6). The thickness determined from our SEM cross-section analyses increases linearly with the d-space distance measured from XRD.

The structural stability of MoS_2 nanolaminates in aqueous solution was examined by successive *ex-situ* XRD measurement at increased soaking time in water as well as in saline solutions (Supplementary Figure 7-9). As shown in **Figure 2f**, the interlayer space of hydrophobic nanochannel is found virtually stable in water for over 100 hours with a swelling of only 8.6%, outperforming GO and MXene membranes (Supplementary Note 2). Our results indicate that stacking functionalized MoS_2 nanosheets into membranes forms stable nanochannels with finely tunable interlayer space and long-term stability. The changes of surface wettability after MoS_2 functionalization were also examined by water contact angle (WCA) measurements (**Fig. 2g** and Supplementary Figure 10, 11). Compared to pristine membranes, increased WCA values were obtained in the case of hydrophobic groups grafted on the MoS_2, whereas hydrophilic groups caused a decrease in the WCA. The measurements of the WCA brings direct evidence of the role of the surface chemistry to change the physical and chemical behavior of the membranes.

Ionic and Water Transport in Functionalized MoS_2 Membranes

We first sought to evaluate the transport of the monovalent ions: Li^+, Na^+ and K^+ across the functionalized MoS_2 membranes using a custom-made U-shape cell, where the two-compartments are filled with an electrolyte solution and DI water, used as permeate and feed solutions, respectively. We found that compared to water, the transport of Na^+ is more sensitive to the height of the 2D capillary, and shows an

exponential dependence with the capillary width (**Fig. 3a** and Supplementary Figure 12). The inhibition of Na^+ transport with decreasing channel size arises from steric hindrance of the pore. The permeation rate for Na^+ decreased by 20 folds as the capillary width decreased from 7.6 Å to 3.6 Å compared to 3 folds for water. In aqueous solution, Na^+, Cl^- and SO_4^{2-} have hydration shells with diameters of 7.16 Å, 6.64 Å and 7.58 Å, respectively[30] . This suggests that to enter inside a narrower channel, the ions will necessarily strip more water molecules, which requires additional energy. It is worth noting that the evolution of the permeation rates of Na^+ with the capillary width, *i.e.* the slopes in the middle and right panels of **Figure 3a**, is independent from the nature of the counter ions (Cl^- or SO_4^{2-}). While the faster permeance of Na^+ (about 3 times) in the case of NaCl compared to Na_2SO_4 is attributed to the larger value of hydration energy for SO_4^{2-}: -1330 kJ mol^{-1} compared to -420 kJ mol^{-1} and -350 kJ mol^{-1} for Na^+ and Cl^-, respectively[31]. We also found slightly higher permeance rates for Mg^{2+} compared to Na^+ despite larger ionic radius. This is attributed to the Gibbs-Donnan effect due to the presence of remaining excess of charges on the functionalized MoS_2 nanolaminates, as confirmed by our zeta potential measurements (Supplementary Table 1). Remarkably, our results also indicated a stricter dependence of the permeance with the capillary width, which is attributed to the larger hydrated radius and hydration energy of the Mg ions.

The application of hydrostatic pressure in reverse osmosis conditions is known to affect the structure of the capillaries in the nanolaminated structure[32,33]. Conversely, by operating in FO, we were able to precisely examine the influence of nanochannel structure and surface chemistry on water permeation. We first evaluated the water permeation across the functionalized MoS_2 membranes with different interlayer spaces under forward osmosis (FO) operation. Concentrated KCl (3M) and deionized (DI)

water were used as draw and feed solutions, respectively. **Figure 3b** shows the water flux across the functionalized membranes with increasing stacking sequence from 160 layers up to 1600 layers in forward osmosis conditions. While pristine membranes were found impermeable[23,34] (Supplementary Note 3), water permeated through all the functionalized MoS_2 nanolaminates, demonstrating the benefit of functionalization for the diffusion of water. The water flux quickly increased with the decrease of stacking layers due to the shortened pathway for water molecules. We found the highest flux of ~12 L h^{-1} m^{-2} (LHM) in the case of Aryl-functionalized membrane with a stacking of 160 layers. This flux is higher than the typical flux for forward osmosis, which is 5~10 LHM[10,35].

We then sought to discriminate the contribution of the capillary width and the surface chemistry of the nanosheets on the water flux. For a fixed number of MoS_2 nanosheets in the nanolaminate, the water flux showed a nearly linear relationship with the capillary width with a ≈3-fold increase when the capillary width increased from 3.6 Å to 7.6 Å. This confirms a size-dependent mass transfer process (Supplementary Figure 14,15 and Supplementary Note 4). We extracted the different slopes values for the functionalized membranes when increasing the number of MoS_2 nanosheets from 160 to 1600. The evolution of the water flux in LMH $Å^{-1}$ with the number of MoS_2 nanosheets revealed an exponential decrease tendency (**Fig. 3b**, inset). According to the curve fitting, our results predict a flux larger than 100 LMH from a nanolaminate membrane with a capillary width of 7 Å and a stacking sequence of 8 layers of MoS_2, corresponding to a thickness of ≈ 10 nm. To better understand the mechanism of water permeation through the size-varied nanochannel, we estimated the activation energy of water permeation[36] and found a linear decrease with capillary width (**Fig. 3c, d** and Supplementary Note 5). Hydrophobic ethyl-functionalized membrane with the

narrowest channel demonstrated the highest transmembrane energy barriers for water permeation in line with the fact that the membrane exhibits the lowest water flux. With the increase of capillary width, the energy barriers rapidly and continuously decrease, leading to improved water flux. Remarkably, we note that the activation energy of water permeation is less affected by the nature of the functional groups (Supplementary Figure 16). The results clearly point out the role of the sub-nanometer interlayer distance for controlling the energy barriers and the water permeance under FO filtration. It is also worth noting that the Aryl-functionalized membranes showed the highest flux for all thicknesses, while it had moderate energy barriers suggesting that the energy barrier is not the only parameter governing water diffusion in nanolaminates.

To elucidate the origin of the apparent high-water flux in Aryl-functionalized MoS_2 membranes, we examined the structure of the nanolaminates by comparing the full-height at half-maximum (FWHM) of (002) XRD peaks. The FHWM of the diffraction peaks is known to be a good indicator of the degree of disorder of a crystal and has been used by extension to qualitatively assess the disorder in 2D nanolaminates[24,37]. The FO membranes made of Aryl-functionalized MoS_2 exhibit the largest FWHM at 1.74° ± 0.03°, indicating a large variation of capillary width of 1.57 Å (Supplementary Figure 17). For comparison, the variation of the capillary width of the corresponding pristine MoS_2 membranes is of only 0.40 Å. The XRD analyses thus suggest a less ordered stacking compared to the other functionalized membranes. A less ordered structure is therefore likely to bring minor tortuosity, leading to a reduced effective path length for water transport, thereby facilitating the water permeation[37]. To further gauge the influence of the stacking disorder on the water diffusion in the nanolaminate, we plotted the water permeance as a function of capillary width and width variation for nanolaminates with 400 and 1600 nanosheets (**Figs. 3e, f**). We observed that for the

thinnest membranes corresponding to a stacking number of 400, the water permeance is controlled by the capillary width, while for thicker laminates the permeance is mainly controlled by the variation in the capillary width. The reduction of the diffusion pathway caused by the decrease of membrane tortuosity is negligible for the thinnest laminates. As the transport pathway increases for thicker membranes, the effect of the tortuosity on the diffusion becomes significant. In light of these results, we identify different behaviors of the nanolaminate FO membranes as the number of two dimensional capillaries increases, which is characterized by a transition from a size-controlled diffusion for the thinnest membranes to disorder-controlled diffusion of the water molecules. Our investigations suggest that the control of both the interlayer space and the stacking disorder in Aryl-functionalized MoS_2 nanolaminates is responsible for the superior water flux in FO, making this membrane a relevant candidate for the realization of practical FO filtration.

Mechanical properties of MoS_2 membranes from MD simulations

The stacking order of the nanolaminate membranes is directly related to the mechanical properties of the layers. Therefore, to get further insight on the atomic origin of the superior water flux of Aryl-functionalized membranes observed above, we performed classical MD simulations of the interaction between functionalized layers (details in the Methods section). Mechanical properties including surface energy and interlayer stiffness can be evaluated by fitting the potential energy of two functionalized layers as a function of interlayer distance, as depicted in **Figure 4a**. Here we use a simple 3-parameters Morse function to fit the potential energy. Our calculations predict surface energies (D_e) of 24, 9 and 6 meV/ $Å^2$, and interlayer stiffnesses (k_e) of 113.7, 11.1 and 5.6 eV/ $Å^2$ for pristine, Ben- and Aryl-functionalized MoS_2, respectively (see **Fig. 4b**

and **c**). We obtained capillary width ($\delta=d_0$-6.15, **Fig. 4d**) of 0.3, 7.4 and 7.8 Å for pristine, Ben- and Aryl-functionalized MoS_2, respectively, in good agreements with those measured from experiment (0.05, 6.9 and 7.1 Å, **Fig. 2d**). As expected, functionalization leads to larger interlayer spacing, smaller surface energy as well as smaller interlayer stiffness. Interestingly, we found that for Aryl- functionalized MoS_2, both the surface energy and the interlayer stiffness are about 50 % smaller than for Ben-MoS_2. The small surface energy and the softness of Aryl-MoS_2 layers can be appreciated by the small depth and the flat bottom of the potential well, respectively (**Fig. 4a**). The combination of small surface energy and interlayer stiffness leads to an increase of stacking defects, which contributes to the broadening of the diffraction peaks measured experimentally. We also performed simulations with a lower extent of functional groups and found that the mechanical properties were only slightly affected, while the capillary width decreased significantly (Supplementary Table 2). Our molecular analysis suggests a direct connection between surface chemistry of the nanosheets and the macroscopic nanofluidic properties of the membranes and it provides a framework for future screening of efficient functional groups for water filtration and desalination.

Forward Osmosis Nanofiltration

To demonstrate the potential of the functionalized MoS_2 membranes, the molecular sieving performance for micropollutants and salt were further evaluated. Four typical micropollutants, a preservative (benzoic acid, BA), a psychoactive drug (caffeine), a common drug (diclofenac sodium, DF) and an organic dye (phthalocyanine), with varied Stoke diameter from ~5.64 Å up to ~14 Å (Supplementary Table 3), were selected and the rejection was measured using high performance liquid chromatography.

Rejections of over 90% for all the micropollutants in functionalized membranes were measured, suggesting excellent separation performance in FO. Particularly, the C_2-functionalized membrane with the narrowest channel presented the perfect repulsion of ≈ 100% for the four selected micropollutants. **Figure 5a** shows that the membrane rejection improves with the increase of the molecular weight of the micropollutants in line with the size-limited diffusion as the primary sieving mechanism (Supplementary Note 6). When comparing the evolution of the rejection of the micropollutant with the capillary width, we observe a sharp molecular cut-off of the FO MoS_2 membranes (**Fig. 5b, c**). This behavior highlights the importance of controlling the interlayer space and further evidences the absence of pinholes. To benchmark the performance of the functionalized MoS_2 membranes, we also estimated the separation performance of the graphene oxide (GO) nanolaminates and a commercial polymeric FO membrane (Cellulose Triacetate, CTA) under the same conditions. As shown in **Figure 5d**, the CTA membrane exhibited both a reduced flux and rejection for the smaller contaminants. We determined a rejection of less than 80% for benzoic acid (BA) in agreement with previous reports from the literature[38]. Both the rejection and the water permeance rapidly increase when filtering large molecules. This behavior is surprisingly the opposite to those of both GO and MoS_2 FO membranes, which showed a decreased rejection and an increased flux for the smaller micropollutants. The decreased performance for sieving out the smallest molecules hints for a rapid fouling due to the blocking of the one-dimensional nanopores of the polymer membranes. Conversely, nanolaminates exhibit a fouling for the largest molecules due to the deposition of the rejected molecules on the surface of the membranes, while the 2D capillaries are not obstructed (Supplementary Figure 18). The surface fouling of the nanolaminate can however be mitigated by operating under tangential crossflow

filtration (as described later in the article). GO membranes also exhibited a poor rejection of 65% for the smallest molecules of BA which is attributed to the large capillary width due to swelling. Overall, owing to the tailored and stable interlayer space, the Aryl-functionalized MoS_2 membranes exhibited superior performance both in rejection and flux than GO and commercial polymer membranes.

To properly estimate the molecular weight cutoff (MWCO) of the MoS_2 membranes, we evaluated the rejection performance of the nanolaminates for small neutral compounds: PEG 200 and D-Glucose. As show in **Figure 6a-c**, all the functionalized MoS_2 membranes exhibited high separation performance with rejection greater than 92%, demonstrating excellent cutoff for PEGs and sugar molecules (Supplementary Note 7).

We then examined the performance of the Aryl-functionalized MoS_2 membranes towards desalination under realistic conditions. FO nanolaminated membranes were prepared by vacuum filtration with sizes up to 45 cm^2 and a stacking of 400 layers, corresponding to a thickness of ≈ 550 nm. We studied the pure water permeance of the planar 45 cm^2 Aryl-functionalized membranes by employing a 2M sucrose as draw solution. A stable water flux of 1.3 LMH was achieved under constant flow conditions at room temperature for a period of 7 days (Supplementary Figure 19). The desalination performance of the functionalized MoS_2 membranes was further evaluated on a pilot-scale tangential flow filtration cell under the forward osmosis operation using 0.1 M NaCl as the feed solution (**Fig. 6d**). A water flux greater than 1.6 LMH was achieved and was largely stable over a 7-day period, whereas salt rejection was maintained at greater than ≈ 94.2% and peaked at 96%. These robust desalination properties are attributed to the control of the interlayer distance from the grafted functional groups

and the low interlayer stiffness. Remarkably, the interlayer space after 7 days of continuous operation was almost identical to that of the as-prepared membranes (Supplementary Figure 20). We note that the performance is slightly lower than those obtained using smaller membranes, which demonstrated a water flux of 4.37 LMH with a NaCl rejection of 93.9% suggesting that further improvements can be achieved. We also evaluated the performance of GO membranes and obtained a poor salt rejection of less than 50 % due to the large capillary width of 12.8 Å in line with the literature (Supplementary Figure 8)[10]. Importantly, the GO membrane could only run for one day and then rapidly delaminated upon the application of the tangential flow which highlights their intrinsic instability in water[39]. Besides, commercial CTA polymer membranes exhibited a rejection of around 89.1% with an average flux of 1.25 LMH when tested under the same conditions– consistent with previous reports[40,41]. Compared with other 2D laminar membranes, the functionalized MoS_2 membranes exhibit a higher water flux and superior salt rejection, exceeding the latest upper bound of state-of-the-art 2D laminar membranes (**Fig. 6e**). Importantly the desalination performance is not significantly affected by the upscaling process and the Aryl-functionalized MoS_2 membranes clearly outperform the best desalination performance from the literature under forward osmosis operation (**Fig. 6f**). We finally evaluated the specific energy consumption (SEC) of our FO system (Supplementary Note 8). Under a flow rate of 3.75 mL min^{-1} (1.65 cm s^{-1}), the FO system recovered 148 mL of water in 20 h, corresponding to a SEC of 0.004 kWh m^{-3}. This value is lower than previous reports for flat-sheet CTA membranes, which exhibit SECs of 0.008 kWh m^{-3} and 0.02 KWh m^{-3}, respectively[42,43]. Although additional processing of the draw solution is requested to obtain potable water, the present FO system shows a clear reduction of the energy footprint compared to the other water recovery approaches such as traditional RO

filtration (1.5-2.5 kWh m^{-3})[44,45], thermal distillation technology (16.3-27.3 kWh m^{-3})[44], and self-supplied FO with thermolytic ammonium bicarbonate (0.1 kWh m^{-3})[46].

Overall this work presents a robust and scalable method to prepare stable nanolaminated membranes with tunable sieving performance and high water permeance in FO filtration. The structure of the functionalized MoS_2 membranes can be precisely adjusted over a large range of interlayer spaces using alkyl and aryl groups which offers ångström-precision for the 2D nanochannels. Using this approach, we elucidated the contributions from the surface chemistry, the interlayer space and the stacking tortuosity on the behavior of FO nanolaminate membranes. Our functionalized membranes exhibit excellent water purification performance compared with the GO and commercial membranes. In particular, we identified Aryl-functionalized MoS_2 membranes as promising candidates for FO application and demonstrated its scalability up to 45 cm^2.

Methods

Preparation of single-layer MoS_2 nanosheets. The single-layer MoS_2 nanosheets were obtained by exfoliating the bulk MoS_2 powder using the lithium intercalation method. Typically, 400 mg MoS_2 powder and 4 mL n-butyllithium were mixed up in hexane solution and the mixture was stirred at 65°C for 48 h under argon protection. After that, the intercalated powders were collected by vacuum filtration and washed with excessive hexane to remove the unreacted reagent. Then the Li-intercalated powder was added to the water for exfoliation and the process was accelerated by the sonication. After one-

hour sonication, the solution was further centrifuged two times at 10,000 g to strip the lithium cations from the nanosheets. In the end, the supernatant containing the single-layer MoS_2 nanosheets was collected after centrifugation twice at 1,400 g for 30 min.

Covalent functionalization of single-layer MoS_2 nanosheets. The single-layer MoS_2 nanosheets were modified in solution by reacting with organohalide reagents and diazonium. Six different molecules were selected: iodoethane, 1-iodopropane, ethyl iodoacetate, (2-iodoethyl) benzene, 3-iodo-1-propanol, and 4-bromobenzenediazonium. First, dimethyl sulfoxide (DMSO) was added to the MoS_2 solution to achieve a volume ratio of 3:2. Then the organohalide reagents or diazonium were directly added to the mixture to react for 48h. The excessive organohalide reagents with ten times fold in molar ratio than MoS_2 was added. While the charged diazonium with the same molar amount as MoS_2 was separately added several times to avoid the electrostatic quench and aggregation. Finally, the functionalized MoS_2 solutions were obtained.

Preparation of functionalized MoS_2 membranes. Vacuum filtration was employed to prepare the laminated membranes using diluted functionalized MoS_2 solution. Briefly, a certain amount of MoS_2 solution was filtered on Nylon filter paper with a pore size of 220 nm. To improve the uniformity of the nanolaminate, polyethersulfone (PES, 50 nm pore size) was used to prepare membranes larger than 10 cm^2. After filtration, the membranes were carefully washed 3 times to remove the unreacted reagents. The prepared membranes were dried at room temperature over 24 h.

Water permeation through nanolaminated MoS_2 membranes. The pure water flux of nanolaminated MoS_2 membranes was measured using the forward osmosis devices, which consist of two compartments filled with equal volumes (40 mL) of salt solution (3 M KCl) and pure water. The MoS_2 membranes were placed in the middle to separate those two compartments. The volume of salt solution as a draw solution would increase

due to the passed water. Based on the increased volume (ΔV) with permeation time (Δt), the water flux could be calculated following the equation:

$$J_w = \frac{\Delta V}{A \Delta t} \quad (2)$$

Where the A is the effective membrane area (1.13 cm^2).

Ionic permeation through the nanolaminated MoS_2 membranes. The Na^+/Mg^{2+} permeation through the 400-layer stacked membranes was measured using two Teflon-made compartments, which were filled with the same volume of DI water and 1 M NaCl/$MgCl_2$ or 0.5 M Na_2SO_4 solution, respectively. Magnetic stirring was used all the time to eliminate possible concentration gradients around the membranes. The conductivity of the feed side was recorded as a function of permeation time. According to the measured conductivity, the salt concentration of feed side could be calculated using the following equation:

$$C = \frac{\kappa}{\Lambda_m} \quad (3)$$

where C denotes the salt concentration, κ presents the measured conductivity and Λm is the molar conductivity (NaCl: 126.4 S cm^2 mol^{-1}, $MgCl_2$: 258.6 S cm^2 mol^{-1}, Na_2SO_4: 259.8 S cm^2 mol^{-1})[47]. The salt permeation rate (J) was calculated by:

$$J = \frac{VC}{At} \quad (4)$$

where V is the solution volume in the feed side (200 mL), C is the calculated concentration from equation (3), A is the surface area of the membrane and t is the permeation time.

Water purification and rejection evaluations. The water purification performances of the membranes were measured using the same apparatus as for the water permeation measurements. However, the draw side and feed side were filled with 2 M sucrose solution and 50 mM micropollutant solution (except for the dye solution, which was

3.3 mM), respectively. The two sides were constantly stirred to avoid the concentration polarization. The draw side solution was collected after 20 h and the concentration of micropollutant in sucrose solution was quantitatively analyzed by High-Performance Liquid Chromatography-Ultraviolet (HPLC-UV). The flux was calculated by equation (2) and the rejection was evaluated by the following equation:

$$R\ (\%) = \frac{C_F - C_P}{C_F} \times 100 \quad (5)$$

Where C_F and C_P denote the concentration of the feed and permeate solutions, respectively. Unlike the reverse osmosis experiments, the permeated solution in forward osmosis system was diluted by the draw solution. The real concentration of the permeated solution was calculated using the following equation to eliminate the dilution effects:

$$C_p = \frac{C_D \times V_D}{V_P} \quad (6)$$

Where C_D and V_D are the measured micropollutant concentration in the draw side and the volume of the draw solution. The V_P presents the volume of permeated solution, which is the increased volume in the draw side.

Water desalination in tangential cross-flow filtration cell. We used the tangential cross-flow filtration cell to estimate the water desalination performance of membranes in long-term operation. The membranes with large surfaces prepared on the polyethersulfone (PES) substrates were installed in the middle of the pilot-scale forward filtration unit to separate the flowing draw and feed solution. The draw and feed tank were filled with 2 M sucrose solution and 0.58 wt.% NaCl solution, respectively. A peristaltic pump was utilized to provide a constant flow rate of 3.75 mL min^{-1}. Two balances were used to monitor the mass changes of draw and feed tank and the recorded data was further used to calculate the flux. The solutions in the tank were

refreshed every 20 h. At the same time, the sucrose solution was collected and the salt concentration was analyzed by Inductively Coupled Plasma Optical Emission Spectrometry (ICP-OES). According to the increased mass and salt concentration in draw side, the salt rejection could be calculated using equations (5) and (6).

Molecular dynamics simulations parameter. Molecular dynamics simulations have been performed with the LAMMPS package[48] and the OPLS interatomic potential[49]. To describe Mo-S interactions, we use the potential proposed by Blankschtein[50]. We developed OPLS parameters (harmonic bonds, harmonic angles and dihedrals) for S-C interactions between fixed MoS_2 and various organic functional groups. We used a Monte Carlo procedure (similar to that presented in Ref. 51) to optimize OPLS parameters against a training set of density functional theory calculations, as developed in the Supplementary file. Molecular models consist of 2 layers of T' MoS_2 replicated 8 and 14 times in the x and y directions, starting from the rectangular unit cell. Functionalization was achieved by randomly grafting functional groups to S atoms until the fraction of 20% groups/S was reached. In order to obtain good statistics on the data points corresponding to the potential energy surface shown in **Figure 4**, we scanned 4 times successively the interlayer distance (back and forth). One potential energy surface corresponds therefore to 8 times (4 times back and forth) 300 interlayer distances. At each interlayer distance, the functional groups were randomized by performing 10 ps of NVT simulation at 600 K followed by an energy minimization. We used high temperature MD to provide efficient randomization of the functional groups at each interlayer distances. Although our force field could be used with a larger timestep, we chose a timestep of 0.5 fs in order to properly integrate the equations of motion in the rough conditions of the simulations.

Data availability

The data that support the plots within this paper and other findings of this study are available from FigShare (https://doi.org/10.6084/m9.figshare.21901638.v1).

Acknowledgments

This research study was supported by the French National Agency (ANR, program 2D-MEMBA - ANR-21-CE09-0034-01). D.V., K.Q., and H. W. acknowledge funding from the European Research Council (ERC) under the European Union's Horizon 2020 research and innovation programme (grant agreement no. 804320). W.W., J.Liu and J.Li acknowledge PhD scholarship from the China Scholarship Council (CSC). C.S. acknowledged funding from the French National Agency (ANR, JCJC program, MONOMEANR-20-CE08-0009). K.Q. and Y.Z. acknowledge financial support from the China Postdoctoral Science Foundation (2018M633127) and the Natural Science Foundation of Guangdong Province (2018A030310602). J.Li acknowledge financial support by the National Natural Science Foundation of China (21808134). The French Région Ile de France - SESAME program is acknowledged for financial support (700 MHz NMR spectrometer). This work was granted access to the HPC resources of IDRIS under the allocation 20*21-2022*-A0110913046 and 097535 made by GENCI. L.L. acknowledges funding from the Andalusian regional government (FEDER-UCA-18-106613), the European Union's Horizon 2020 research and innovation program

(grant agreement 823717 – ESTEEM3) and the Spanish Ministerio de Economia y Competitividad (PID2019-107578GA-I00). The (S)TEM measurements were performed at the National Facility ELECMI ICTS ("Division de Microscopia Electronica", Universidad de Cadiz, DME-UCA).

Author Contributions

D.V. conceived the idea, designed the experiments and wrote the manuscript. W.W. designed the experiments with D.V., synthesized the functionalized nanosheets, fabricated the membranes and performed the experiments. D.V. and W.S. analyzed the data and wrote the manuscript. N.O. performed the atomistic calculations and discussed the results with D.V. and W.W.. B.A.K. assisted W.S. with the measurements and synthesized MXene. E.P. performed the liquid NMR and HPLC-UV to quantify the membrane rejection, while H.W., J.Liu, J.Li, K.Q. and Y.Z. and assisted W.W with the WCA, Raman, FTIR measurements. L.L. performed the (S)TEM measurements and analyzed the data. C.G. performed the solid ^{13}C NMR spectroscopy measurements and discussed with results with C.S.. P.M. and Z.Z. discussed the results with W.W. and D.V. All of the authors edited the manuscript before submission.

Competing financial interests

The authors declare no competing financial interests.

Additional Information

Supplementary information and chemical compound information are available in the online version of the paper.

Correspondence and requests for materials should be addressed to D.V. (damien.voiry@umontpellier.fr).

Figure 1 | Characterizations of the functionalized MoS_2 nanosheets. a, High-angle annular dark-field (HAADF) STEM image of 4-bromobenzenediazonium salt functionalized MoS_2 nanosheets and the corresponding EDX mapping for elements Br (in red) and S (in blue). The elemental mapping of Br in the functionalized MoS_2 nanosheets shows that the aryl groups are homogeneously grafted on the nanosheets surface. **b**, HRTEM images of MoS_2 nanosheets functionalized with aryl groups. The vertically aligned nanosheets form an interlayer spacing of ~13.2 Å, in line with the XRD measurements. Meanwhile, the crystalline nature of the basal plane of Aryl-MoS_2 nanosheets is confirmed by the diffraction pattern (inset). **c**, The SEM cross-section view of laminated membrane prepared by vacuum filtration of Aryl-MoS_2 nanosheets suspension. The highly aligned nanosheets in the vertical direction form 2D capillaries.

Figure 2 | Characterization of the functionalized MoS_2 membranes. a and **b**, ^{13}C CP MAS NMR spectra of the Ace-functionalized (**a**, bottom) and Aryl-functionalized (**b**, bottom) MoS_2 nanosheets. ^{13}C NMR spectra of pure chemical reagents namely ethyl iodoacetate (**a**, top, solution) and 4-bromobenzenediazonium (**b**, top, solid-state) were also recorded for comparison. The color dots are used to point out the positions of carbon atoms in different chemical environments. **c**, Schematic illustration of the separation process of stacked functionalized MoS_2 membranes with varied capillary width for water purification and desalination. The values marked in the nanochannels represent the effective layer space in aqueous solution through which water molecules can shuttle. Atom color codes: Mo, pink; S, yellow; C, cyan; H, white; O, red; Br, magenta; Na^+, blue; Cl^-, green; Micropollutant, ice-blue; water, transparent gray. **d**, X-

ray diffraction pattern of pristine and functionalized MoS_2 membranes after vacuum drying for 24 h. **e**, Measured thickness of MoS_2 membranes before and after functionalization as a function of d-space. The slope k multiplied by 10 represents the number of stacked layers. **f**, Evolution of the capillary width of functionalized MoS_2 membranes in pure water over the soaking time. **g**, The contact angle of pristine and functionalized MoS_2 membranes. Data are presented as mean values. All error bars correspond to standard deviations (SD) based on at least three independent measurements.

Figure 3 | Water permeation and ionic transport. a, The Na^+/Mg^{2+} permeation rates and water flux measured by using 400-layer stacked membranes at room temperature. 1 M $NaCl/MgCl_2$ or 0.5 M Na_2SO_4 were employed to provide the high ionic strengths (1 M Na^+/Mg^{2+}) for diffusion. The Na^+/Mg^{2+} permeation rate depends exponentially on the capillary width while the water flux varies linearly. Error bars are omitted for clarity. The dotted lines are best fits. **b**, Water flux of functionalized MoS_2 membranes with different stacking layers measured at room temperature under forward osmosis, where 3M KCl and DI water were used as the draw and feed solution, respectively. Inset: the water permeance as a function of membrane thickness. The red curve is the best fit. **c**, Temperature dependence of water permeation of 400-layer stacked membranes. Solid lines are best fits to Arrhenius activation energies. **d**, Activation energy of water permeation for the functionalized MoS_2 membranes as a function of capillary width. The activation energy varied linearly with capillary width. The dotted line is the best fit. Horizontal error bars represent the average half-height of the XRD peaks measured after immersing the membranes in water for a long time (Supplementary Figure 7). **e-f**, The plotted water permeance of membranes with different stacking numbers (400 layers in **e** and 1600 layers in **f**) as a function of capillary width and width variation (Supplementary Figure 17). The permeation rates were normalized by the permeance of Aryl-functionalized MoS_2 membranes. All vertical error bars correspond to SD and based on at least five independent measurements.

Figure 4 | Mechanical properties of functionalized MoS_2 nanosheets. a, Potential energy as a function of interlayer separation. To obtain reliable data and statistics, the potential energy surface was scanned 4 times back and forth, as described in the Methods section. Dots correspond to averaged data points and some error bars are displayed (one error bar every 10 averaged data points). Lines correspond to Morse fits

as defined by the equation $U(d) = D_e(1-\exp(-\alpha(d-d_0)))^2$. **b**, Surface energy (D_e). **c**, Interlayer stiffness ($k_e = 2D_e\alpha^2$). **d**, Experimental capillary width as a function of those (d_0-6.15) extracted from the Morse fit.

Figure 5 | Water purification performance of the functionalized MoS_2 membranes. **a**, Trace organic contaminants rejection measured with 400-layer stacked functionalized MoS_2 membranes at 30°C under forward osmosis, where the 2 M sucrose and 50 mM contaminants (3.3 mM for dye) were used as draw and feed solution. The rejection is plotted as a function of the molecular weight of contaminants. Vertical error bars represent SD of at least five independent measurements. The insets show the molecular structure of contaminants and the gray, white, red, blue, green and yellow balls denote C, H, O, N, Cl and S, respectively. **b** and **c**, Evolution of the rejection for the benzoic acid (**b**) and caffeine (**c**) with the capillary width of membranes. The dotted lines represent the effective hydrodynamic diameter of contaminant molecules (Stokes diameter). The rejection sharply decreases after the capillary width of membranes are larger than the effective diameter of the micropollutants, showing size-selective sieving. The solid gray lines are guides to the eyes. **d**, Comparison of the water purification performance from the functionalized MoS_2 membranes with GO and commercial FO membrane (CTA). Each symbol represents the average flux and rejection calculated from at least five independent measurements and the error bars are omitted for clarity. The complete test data of all functionalized MoS_2 membranes are shown in Supplementary Figure 18.

Figure 6 | Molecular weight cut-off and water desalination performance of the functionalized MoS_2 membranes. Evolution of the rejection for the PEG-238 (**a**), PEG-282 (**b**) and D-Glucose (**c**) with the capillary width of membranes. The rejection was measured with 400-layer stacked functionalized MoS_2 membranes at 30 °C under forward osmosis, where the 2 M sucrose/50 mM PEG 200 and 0.92 M Na_2SO_4/50 mM D-Glucose were used as draw/feed solution, respectively. Error bars correspond to SD of at least five independent measurements. The dotted lines represent the effective hydrodynamic diameter of PEG and D-Glucose (Stokes diameter). And the solid gray lines are guides to the eyes. **d**, The desalination performance of Aryl-functionalized MoS_2 membrane and the comparison with GO and commercial FO membrane. The measurements were conducted in a tangential cross-flow cell using 2 M sucrose and 0.1 M NaCl as draw and feed solution. The GO membrane could only be run for one day

and then decomposed. **e**, Comparison of the desalination performance of Aryl-functionalized MoS_2 (red stars) with other 2D laminar membranes made of GO, MXene and their hybrids. All the data listed in the figure were measured under separation models in forward osmosis cells using sucrose and 0.1 M NaCl as draw and feed solution. Our Aryl-functionalized MoS_2 membranes test data are marked with red stars, while CTA and GO data are denoted by light-blue and green hollow diamonds. The effective membrane area is labeled in white. The black line represents the upper bound of state-of-the-art 2D laminar membranes due to the trade-off between membrane permeability and selectivity. A comprehensive comparison of desalination performance of 2D membranes estimated under diffusion or separation models can be found in Supplementary Table 5. **f**, Comparison of effective membrane area measured in our work with previously reported membranes.

Figure1

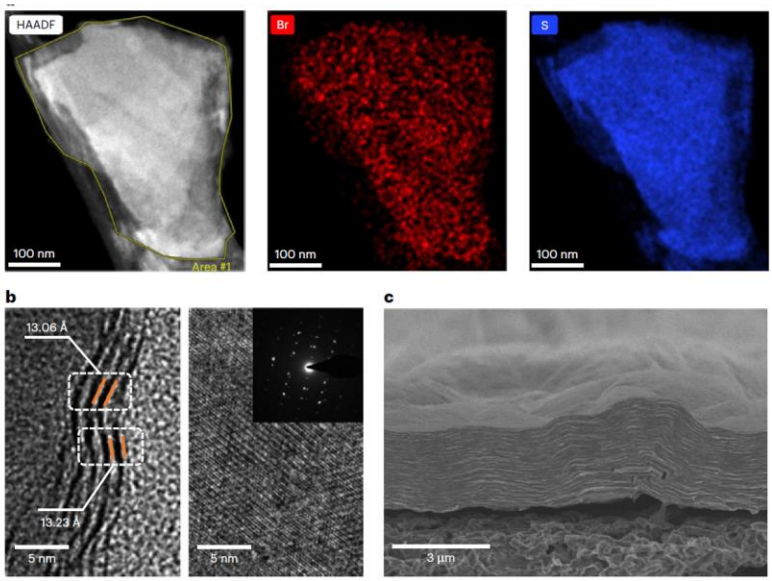

662

Figure2

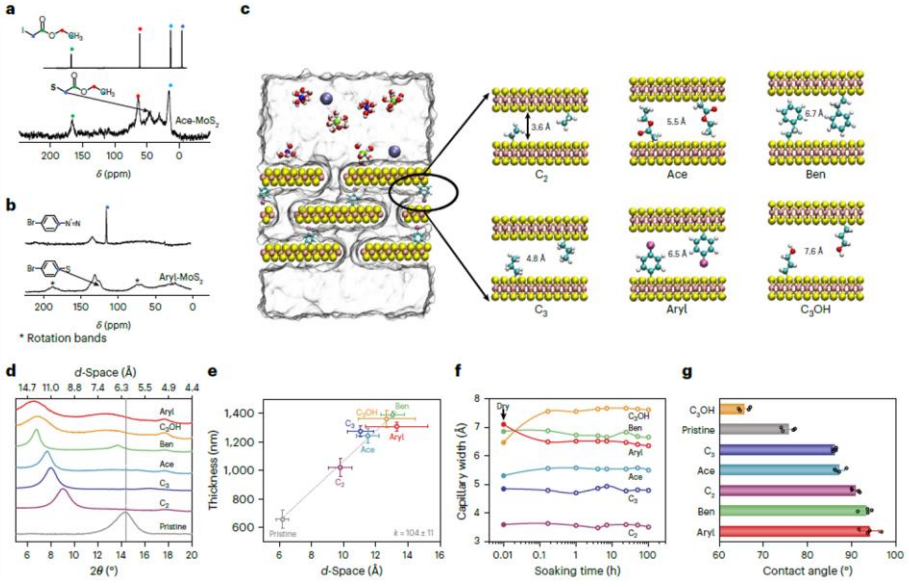

663

Figure3

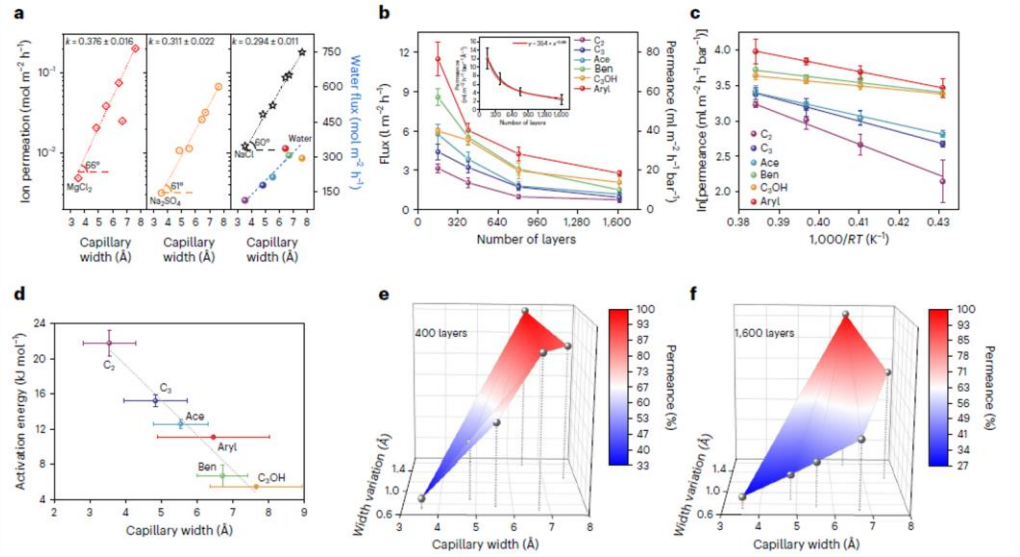

664

Figure4

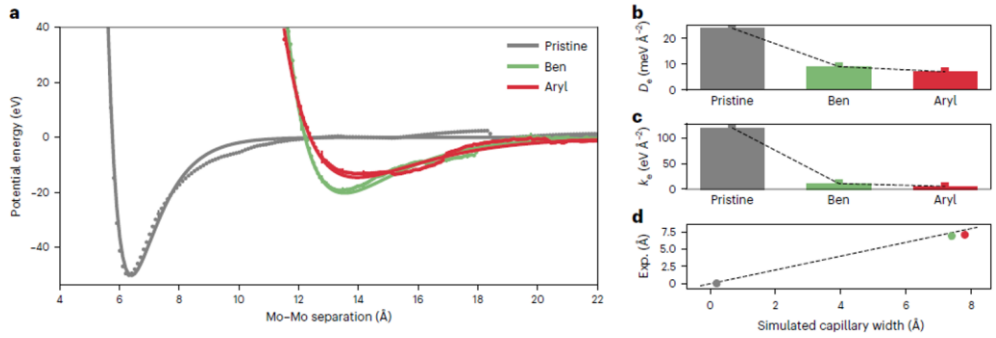

665

Figure5

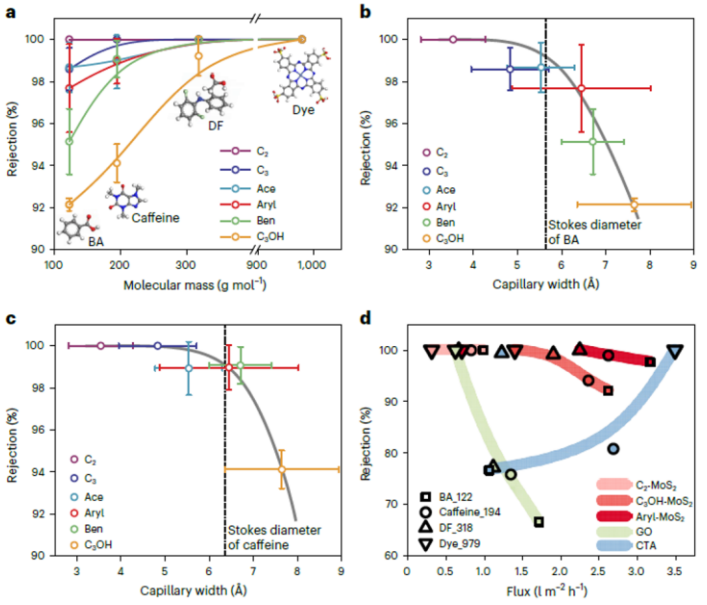

666

Figure6

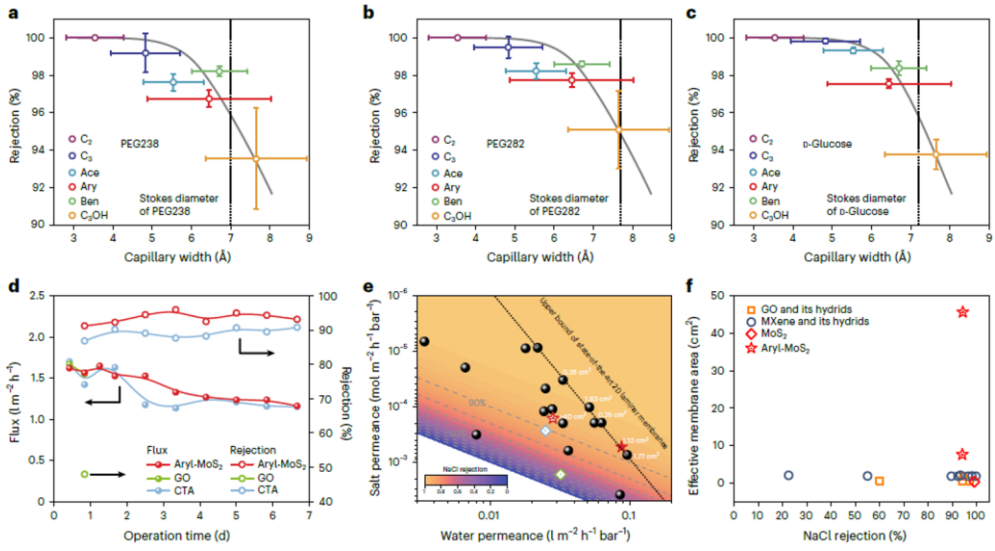

667

668

References

1 Shen, J., Liu, G., Han, Y. & Jin, W. Artificial channels for confined mass transport at the sub-nanometre scale. *Nat. Rev. Mater.* **6**, 294-312 (2021).

2 Werber, J. R., Osuji, C. O. & Elimelech, M. Materials for next-generation desalination and water purification membranes. *Nat. Rev. Mater.* **1**, 1-15 (2016).

3 Wang, S. *et al.* Two-dimensional nanochannel membranes for molecular and ionic separations. *Chem. Soc. Rev.* **49**, 1071-1089 (2020).

4 Kang, Y., Xia, Y., Wang, H. & Zhang, X. 2D laminar membranes for selective water and ion transport. *Adv. Funct. Mater.* **29**, 1902014 (2019).

5 Cheng, L., Liu, G., Zhao, J. & Jin, W. Two-dimensional-material membranes: Manipulating the transport pathway for molecular separation. *Acc. Mater. Res.* **2**, 114-128 (2021).

6 Safaei, J., Xiong, P. & Wang, G. Progress and prospects of two-dimensional materials for membrane-based water desalination. *Mater. Today Adv.* **8**, 100108 (2020).

7 Liu, P. *et al.* Two-dimensional material membranes for critical separations. *Inorg. Chem. Front.* **7**, 2560-2581 (2020).

8 Cheng, Y., Pu, Y. & Zhao, D. Two-Dimensional Membranes: New Paradigms for High-Performance Separation Membranes. *Chem. Asian J.* **15**, 2241-2270 (2020).

9 Joshi, R. *et al.* Precise and ultrafast molecular sieving through graphene oxide membranes. *Science* **343**, 752-754 (2014).

10 Abraham, J. *et al.* Tunable sieving of ions using graphene oxide membranes. *Nat. Nanotechnol.* **12**, 546-550 (2017).

11 Chen, L. *et al.* Ion sieving in graphene oxide membranes via cationic control of interlayer spacing. *Nature* **550**, 380-383 (2017).

12 Shen, J. *et al.* Subnanometer two-dimensional graphene oxide channels for ultrafast gas sieving. *ACS Nano* **10**, 3398-3409 (2016).

13 Hung, W.-S. *et al.* Cross-linking with diamine monomers to prepare composite graphene oxide-framework membranes with varying d-spacing. *Chem. Mater.* **26**, 2983-2990 (2014).

14 Zheng, S., Tu, Q., Urban, J. J., Li, S. & Mi, B. Swelling of graphene oxide membranes in aqueous solution: characterization of interlayer spacing and insight into water transport mechanisms. *ACS Nano* **11**, 6440-6450 (2017).

15 Su, P., Wang, F., Li, Z., Tang, C. Y. & Li, W. Graphene oxide membranes: controlling their transport pathways. *J. Mater. Chem. A* **8**, 15319-15340 (2020).
16 Han, Z.-y. *et al.* A review of performance improvement strategies for graphene oxide-based and graphene-based membranes in water treatment. *J. Mater. Sci.*, 1-30 (2021).
17 Sun, L., Huang, H. & Peng, X. Laminar MoS_2 membranes for molecule separation. *Chem. Commun.* **49**, 10718-10720 (2013).
18 Guo, B.-Y. *et al.* MoS2 membranes for organic solvent nanofiltration: stability and structural control. *J. Phys. Chem. Lett.* **10**, 4609-4617 (2019).
19 Ren, C. E. *et al.* Charge-and size-selective ion sieving through $Ti_3C_2T_x$ MXene membranes. *J. Phys. Chem. Lett.* **6**, 4026-4031 (2015).
20 Ding, L. *et al.* A two-dimensional lamellar membrane: MXene nanosheet stacks. *Angew. Chem. Int. Ed. Engl.* **56**, 1825-1829 (2017).
21 Wang, J. *et al.* Ion sieving by a two-dimensional $Ti_3C_2T_x$ alginate lamellar membrane with stable interlayer spacing. *Nat. Commun.* **11**, 1-10 (2020).
22 Kim, S., Wang, H. & Lee, Y. M. 2D nanosheets and their composite membranes for water, gas, and ion separation. *Angew. Chem. Int. Ed. Engl.* **131**, 17674-17689 (2019).
23 Wang, Z. *et al.* Understanding the aqueous stability and filtration capability of MoS2 membranes. *Nano Lett.* **17**, 7289-7298 (2017).
24 Ries, L. *et al.* Enhanced sieving from exfoliated MoS_2 membranes via covalent functionalization. *Nat. Mater.* **18**, 1112-1117 (2019).
25 Mei, L. *et al.* Simultaneous Electrochemical Exfoliation and Covalent Functionalization of MoS_2 Membrane for Ion Sieving. *Adv. Mater.*, 2201416 (2022).
26 Chu, C. *et al.* Precise ångström controlling the interlayer channel of MoS_2 membranes by cation intercalation. *J. Memb. Sci.* **615**, 118520 (2020).
27 Eda, G. *et al.* Photoluminescence from chemically exfoliated MoS_2. *Nano Lett.* **11**, 5111-5116 (2011).
28 Creemers, A. F. & Lugtenburg, J. The preparation of all-trans uniformly 13C-labeled retinal via a modular total organic synthetic strategy. Emerging central contribution of organic synthesis toward the structure and function study with atomic resolution in protein research. *J. Am. Chem. Soc.* **124**, 6324-6334 (2002).

29 Duthaler, R. O., Förster, H. & Roberts, J. D. Nitrogen-15 and carbon-13 nuclear magnetic resonance spectra of diazo and diazonium compounds. *J. Am. Chem. Soc.* **100**, 4974-4979 (1978).

30 Nightingale Jr, E. Phenomenological theory of ion solvation. Effective radii of hydrated ions. *J. Phys. Chem.* **63**, 1381-1387 (1959).

31 Teychené, J., Roux-de Balmann, H., Maron, L. & Galier, S. Investigation of ions hydration using molecular modeling. *J. Mol. Liq.* **294**, 111394 (2019).

32 Wei, Y. *et al.* Declining flux and narrowing nanochannels under wrinkles of compacted graphene oxide nanofiltration membranes. *Carbon* **108**, 568-575 (2016).

33 Morelos-Gomez, A. *et al.* Effective NaCl and dye rejection of hybrid graphene oxide/graphene layered membranes. *Nat. Nanotechnol.* **12**, 1083-1088 (2017).

34 Hoenig, E. *et al.* Controlling the Structure of MoS_2 Membranes via Covalent Functionalization with Molecular Spacers. *Nano Lett.* **20**, 7844-7851 (2020).

35 Chekli, L. *et al.* A comprehensive review of hybrid forward osmosis systems: Performance, applications and future prospects. *J. Memb. Sci.* **497**, 430-449 (2016).

36 Wang, K. Y., Chung, T.-S. & Qin, J.-J. Polybenzimidazole (PBI) nanofiltration hollow fiber membranes applied in forward osmosis process. *J. Memb. Sci.* **300**, 6-12 (2007).

37 Lu, X. *et al.* Relating selectivity and separation performance of lamellar two-dimensional molybdenum disulfide (MoS_2) membranes to nanosheet stacking behavior. *Environ. Sci. Technol.* **54**, 9640-9651 (2020).

38 Alturki, A. *et al.* Performance of a novel osmotic membrane bioreactor (OMBR) system: flux stability and removal of trace organics. *Bioresour. Technol.* **113**, 201-206 (2012).

39 Andreeva, D. V. *et al.* Two-dimensional adaptive membranes with programmable water and ionic channels. *Nat. Nanotechnol.* **16**, 174-180 (2021).

40 Al-aibi, S., Mahood, H. B., Sharif, A. O., Alpay, E. & Simcoe-Read, H. Evaluation of draw solution effectiveness in a forward osmosis process. *Desalination Water Treat.* **57**, 13425-13432 (2016).

41 Li, G., Li, X.-M., He, T., Jiang, B. & Gao, C. Cellulose triacetate forward osmosis membranes: preparation and characterization. *Desalination Water Treat.* **51**, 2656-2665 (2013).

42 Zou, S. & He, Z. Enhancing wastewater reuse by forward osmosis with self-diluted

commercial fertilizers as draw solutes. *Water Res.* **99**, 235-243 (2016).

43 Lambrechts, R. & Sheldon, M. Performance and energy consumption evaluation of a fertiliser drawn forward osmosis (FDFO) system for water recovery from brackish water. *Desalination* **456**, 64-73 (2019).

44 Al-Karaghouli, A. & Kazmerski, L. L. Energy consumption and water production cost of conventional and renewable-energy-powered desalination processes. *Renew. Sustain. Energy Rev.* **24**, 343-356 (2013).

45 Shannon, M. A. *et al.* Science and technology for water purification in the coming decades. *Nanoscience and technology: a collection of reviews from nature Journals*, 337-346 (2010).

46 Qin, M. & He, Z. Self-supplied ammonium bicarbonate draw solute for achieving wastewater treatment and recovery in a microbial electrolysis cell-forward osmosis-coupled system. *Environ. Sci. Technol. Lett.* **1**, 437-441 (2014).

47 Horvath, A. L. *Handbook of aqueous electrolyte solutions*. (Halsted Press, 1985).

48 Plimpton, S. Fast parallel algorithms for short-range molecular dynamics. *J. Comput. Phys.* **117**, 1-19 (1995).

49 Jorgensen, W. L., Maxwell, D. S. & Tirado-Rives, J. Development and testing of the OPLS all-atom force field on conformational energetics and properties of organic liquids. *J. Am. Chem. Soc.* **118**, 11225-11236 (1996).

50 Sresht, V. *et al.* Quantitative modeling of MoS_2–solvent interfaces: predicting contact angles and exfoliation performance using molecular dynamics. *J. Phys. Chem. C* **121**, 9022-9031 (2017).

51 Onofrio, N. & Ko, T. W. Exploring the Compositional Ternary Diagram of Ge/S/Cu Glasses for Resistance Switching Memories. *J. Phys. Chem. C* **123**, 9486-9495 (2019).